




Article

Enhancing Interaction between Lanthanum Manganese Cobalt Oxide and Carbon Black through Different Approaches for Primary Zn–Air Batteries

Mario García-Rodríguez ¹, Jhony X. Flores-Lasluisa ¹, Diego Cazorla-Amorós ² and Emilia Morallón ^{1,*}

¹ Departamento Química Física e Instituto Universitario de Materiales, Universidad de Alicante, Ap. 99, E-03080 Alicante, Spain; mario.garcia@ua.es (M.G.-R.)

² Departamento Química Inorgánica e Instituto Universitario de Materiales, Universidad de Alicante, Ap. 99, E-03080 Alicante, Spain; cazorla@ua.es

* Correspondence: morallon@ua.es

Abstract: Due to the need for decarbonization in energy generation, it is necessary to develop electrocatalysts for the oxygen reduction reaction (ORR), a key process in energy generation systems such as fuel cells and metal–air batteries. Perovskite–carbon material composites have emerged as active and stable electrocatalysts for the ORR, and the interaction between both components is a crucial aspect for electrocatalytic activity. This work explores different mixing methods for composite preparation, including mortar mixing, ball milling, and hydrothermal and thermal treatments. Hydrothermal treatment combined with ball milling resulted in the most favorable electrocatalytic performance, promoting intimate and extensive contact between the perovskite and carbon material and improving electrocatalytic activity. Employing X-ray photoelectron spectroscopy (XPS), an increase in the number of M–O–C species was observed, indicating enhanced interaction between the perovskite and the carbon material due to the adopted mixing methods. This finding was further corroborated by temperature-programmed reduction (TPR) and temperature-programmed desorption (TPD) techniques. Interestingly, the ball milling method results in similar performance to the hydrothermal method in the zinc–air battery and, thus, is preferable because of the ease and straightforward scalability of the preparation process.

Keywords: perovskite; carbon material; composites; ORR; synergistic effect; strong interaction



Citation: García-Rodríguez, M.; Flores-Lasluisa, J.X.; Cazorla-Amorós, D.; Morallón, E. Enhancing Interaction between Lanthanum Manganese Cobalt Oxide and Carbon Black through Different Approaches for Primary Zn–Air Batteries. *Materials* **2024**, *17*, 2309. <https://doi.org/10.3390/ma17102309>

Academic Editors:

Esther Bailón-García,
María Pérez-Cadenas and
Abdelhakim Elmouwahidi

Received: 12 April 2024

Revised: 8 May 2024

Accepted: 9 May 2024

Published: 13 May 2024



Copyright: © 2024 by the authors. Licensee MDPI, Basel, Switzerland. This article is an open access article distributed under the terms and conditions of the Creative Commons Attribution (CC BY) license (<https://creativecommons.org/licenses/by/4.0/>).

1. Introduction

Climate change is a major concern today due to the high levels of pollution from fossil fuels. To address this challenge, society needs to transition towards a renewable and sustainable energy model [1,2]. Therefore, developing systems to store and convert energy from renewable sources is crucial. Electrochemical devices including fuel cells and primary metal–air batteries (ZABs) are potential candidates to meet this purpose [3,4]. ZABs have received intensive research and development activity because of their high theoretical energy density (1086 Wh/kg), abundant reserves of Zn metal, good rechargeability, low manufacturing cost, high safety, and eco-friendliness [5,6]. An additional key advantage of ZABs is their compatibility with other energy storage systems. This allows them to leverage complementary technologies, combining the strengths of each system for a more robust and efficient energy storage solution. This makes ZABs highly attractive for commercialization, and they have garnered significant attention from both academia and industry. The past decade has witnessed a surge in ZAB research, as evidenced by the rapidly increasing number of publications [7].

The main limitation for large-scale implementation in primary ZABs is the slow kinetics of the oxygen reduction reaction (ORR) [8–10]. While noble metal catalysts like Pt/C demonstrate excellent ORR activity, their high cost and scarcity render them unsuitable

for large-scale applications. Therefore, research is needed to develop cost-effective electrocatalysts for the ORR. The family of metal oxide perovskites of the AMO_3 type, where A is a rare earth or alkaline earth cation and M is a transition metal cation, is an attractive candidate for this reaction [11,12]. However, limited conductivity hinders their electrocatalytic activity. A solution involves adding a second phase with high electronic conductivity, such as carbon materials. This results in a composite that exhibits significantly enhanced ORR activity compared to the pure perovskite-type metal oxide or carbon material alone. This improvement is attributed to a synergistic effect, where the combined phases work together to improve overall performance [13].

Three possible origins could explain the synergistic effect [14,15]. First, the ligand (electron) effect involves the electronic interaction (charge transfer) between two elements. It is widely used in alloys and metal/metal oxide composites for electrocatalysis and heterogeneous catalysis and is the main reason for improving catalytic performance. Thus, the ligand effect at the interface between the carbon material and the perovskite can change the electronic structure and promote electron transfer. Second, the formation of interfacial heterostructures (i.e., covalent bonds or a new phase at the interface), usually represented as M-O-C interactions [16–18], can be at the origin of the synergistic effect for enhanced ORR performance in the strongly coupled hybrids. The M-O-C species are believed to favor the adsorption and desorption of oxygen-containing species from active sites, thereby enhancing the overall reaction [17]. Other authors also relate the improvement in electrocatalytic activity to the intrinsic properties of carbon materials, such as their hydrophobicity, low degree of structural order, surface area, and homogeneity [19,20].

On the other hand, a change in the mechanism by which the ORR takes place in perovskite–carbon composites is also proposed [21]. One possible explanation is that carbon material and perovskite-type metal oxide catalyze different reactions, resulting in a series of 2e^- (carbon material) + 2e^- (perovskite) reactions. The 2e^- reaction of oxygen to hydroperoxide is first catalyzed by carbon material. The hydroperoxide is then desorbed and subsequently adsorbed onto the metal oxide perovskite [22,23]. Then, the perovskite catalyzes the electrochemical reduction of hydroperoxide to hydroxide according to the well-known ORR–perovskite mechanism [24]. While this mechanism appears to be a pseudo- 4e^- pathway, it does not necessarily exclude the possibility of a direct 4e^- reaction occurring simultaneously. Furthermore, there is no evidence that this two-step two-electron mechanism can be applied to all perovskite composites.

There is a wide variety of carbon materials that can be combined with perovskite-type metal oxides, which have demonstrated an improvement in electrocatalytic activity. Carbon black (CB) materials are the most commonly used because they increase the electrical conductivity and even exhibit some inherent ORR activity (some examples are Vulcan XC-72(R) [25–27], acetylene black [28,29], Ketjen black [30], and Super P [31,32]). Several studies have explored incorporating carbon materials with even higher electrical conductivity, such as carbon nanotubes [33,34] and graphene-based materials [35,36], or higher surface areas like activated carbons [37]. Alternatively, some research has focused on nitrogen-doped carbon materials, which possess inherent active sites for the ORR, further enhancing the activity of the metal oxides [38,39].

The way of mixing perovskite-type metal oxides with carbon materials is also a critical aspect affecting the electrocatalytic activity [40]. The most commonly used method involves physical mixing after the synthesis of the metal oxide perovskite [41–43], either using a mortar or specific equipment such as a ball mill. Another approach involves chemical synthesis in the presence of the carbon material. This method aims to create a stronger interaction between the perovskite and the carbon material. The literature explores various chemical synthesis techniques, including the hydrothermal method [39,44,45], electrospinning [46], and chemical vapor deposition (CVD) [47,48]. Some works simply ultrasonicated perovskite and carbon to make the mixture [49], but other works such as the one published by Wang et al. [50] developed a perovskite–carbon Super P composite through ball milling both components for ZAB applications. In addition, hydrothermal treatment has been

used for developing a LaNiO_3 -nanorod/graphene composite for ZAB applications [44]. However, the potential benefits of combining physical and chemical treatments when mixing the two components post-perovskite synthesis have not yet been studied.

This work investigates the electrocatalytic activity of $\text{La}_{0.6}\text{Mn}_{0.7}\text{Co}_{0.3}\text{O}_3$ perovskite for the ORR by incorporating carbon materials through various mixing methods. Prior research has identified $\text{LaMn}_{0.7}\text{Co}_{0.3}\text{O}_3$ as the most electroactive composition in the $\text{LaMn}_{1-x}\text{Co}_x\text{O}_3$ series due to the formation of oxygen vacancies and an enhanced surface concentration of active M-site cations [27]. These vacancies act through a charge compensation mechanism, improving overall performance. Additionally, studies on $\text{La}_{1-x}\text{MnO}_3$ oxides suggest that creating A-site vacancies can further increase the concentration of active sites on the surface [51]. Then, the combination of both factors involving M- and A-sites for the ORR in lanthanum manganese cobalt oxides can be interesting in improving the ORR mechanism towards the overall four-electron reaction, and the interaction with carbon material can also be enhanced [52]. Combining these strategies, this work explores the potential benefits of manipulating both M- and A-sites in the $\text{La}_{0.6}\text{Mn}_{0.7}\text{Co}_{0.3}\text{O}_3$ perovskite for improving ORR activity, particularly towards the favorable four-electron reaction pathway. To achieve this, various mixing methods are employed, including the mortar method, ball milling, and a combination of ball milling with low-temperature hydrothermal and high-temperature thermal treatments. Additionally, the most electroactive samples are evaluated in a primary ZAB.

2. Experimental

The materials and reagents used, as well as the characterization techniques, can be found in the Supporting Information.

Synthesis Procedure

The synthesis of $\text{La}_{0.6}\text{Mn}_{0.7}\text{Co}_{0.3}\text{O}_3$ (L6M7C3O) was performed by a sol–gel method similar to that described in the literature [53]. The mass of reagents was adjusted to obtain approximately 1.0 g of product, employing a 1:1.5:1 molar ratio for EDTA, citric acid, and the sum of cation precursors, respectively. The cation molar ratio was adjusted to 0.6:0.7:0.3 for $\text{La}(\text{NO}_3)_3 \cdot 6\text{H}_2\text{O}$, $\text{Mn}(\text{NO}_3)_2 \cdot x\text{H}_2\text{O}$, and $\text{Co}(\text{NO}_3)_2 \cdot 6\text{H}_2\text{O}$, respectively. First, EDTA was dissolved in a mixture of 41 mL of deionized water and 3.3 mL of NH_3 . The stoichiometric amounts of metal precursors and citric acid were added to the EDTA solution. Then, NH_3 was slowly dropped into the solution to set the pH at 9 to form a stable sol complex. Then, the solution was stirred at 80 °C for 6 h and subsequently dried at 150 °C overnight in a stove to obtain the gel. The gel was heated at 500 °C for 1 h. Finally, this product was ground and calcined at 700 °C for 6 h to form the perovskite metal oxide materials.

The metal oxide–carbon material samples were prepared using different methods, with a 1:1 weight ratio between both components. The mortared sample was obtained by mixing both components (metal oxide and carbon black) employing an agate mortar for 15 min (L6M7C3O_Mortar). The ball-milled sample (L6M7C3O_BM) was prepared by mixing both components using a planetary mill Retsch PM 200 under 350 rpm for 30 min, following the milling, using the optimal milling conditions reported in our previous work [40]. The hydrothermal sample (L6M7C3O_HT) was obtained by sonicating 250 mg of the L6M7C3O_BM sample with 28 mL of H_2O and 2 mL of NH_3 for 30 min. Then, the dispersion was transferred to a Teflon reactor and introduced into an autoclave which was kept for 15 h at 150 °C. Finally, the sample was washed until a neutral pH was reached and then dried at 80 °C overnight. The thermally treated sample (L6M7C3O_TT) was obtained by heating 250 mg of the L6M7C3O_BM sample up to 500 °C for 3 h at a heating rate of 5 °C/min under an N_2 atmosphere.

3. Results and Discussion

3.1. Bulk Structure and Composition

In order to investigate the potential impact of the mixing procedure on the electrocatalytic activity, the materials were characterized by TEM microscopy to observe any changes in the perovskite nanoparticles resulting from the mixing procedure. These changes could affect the electrochemical activity. Figure S1 depicts a TEM image of L6M7C3O perovskite, revealing agglomerates of irregularly shaped nanoparticles of around 25 nm. Figure S2 displays the TEM images of the perovskite–carbon composites produced using different methods. The samples exhibit irregular agglomerates of spherical shape, with the perovskite particles retaining their size and shape. The size of the agglomerates varies between samples, with L6M7C3O_Mortar and L6M7C3O_BM samples exhibiting a similar mean diameter of 35 nm, while the mean diameter for the L6M7C3O_HT and L6M7C3O_TT samples is 29 and 57 nm, respectively. These findings demonstrate that hydrothermal treatment reduces the mean diameter of the perovskite–carbon material nanoparticles, while the thermal treatment sinters the nanoparticles.

For optimal catalytic activity, symmetrical crystal structures in the metal oxide are desired. These configurations facilitate the interaction between the reactants and M site cations, which are the active sites for the ORR. X-ray diffraction (XRD) was employed to characterize the crystalline structure of the metal-oxide–perovskite-type materials. The L6M7C3O_Mortar sample was excluded as mortar mixing is known to not alter the crystal structure [40]. Figure 1 displays the XRD patterns obtained for the perovskite-based materials showing peaks at $2\theta = \sim 23, 33, 40, 47, 58,$ and 68° , which correspond to the (0 1 0), (0 1 1), (1 1 1), (0 2 0), (1 2 1), and (0 2 2) planes. These peaks can be indexed to a cubic perovskite phase LaMnO_3 belonging to the Pm-3m space group (PDF code: 96-154-2146). The results confirm the successful incorporation of cobalt into the LaMnO_3 crystal structure since no other cobalt oxides are detected. A magnification of the XRD signal in the region $32\text{--}33^\circ$ (Figure 1b) reveals a slight shift in the diffraction peak towards lower values of 2θ in the samples mixed with carbon, compared to the pure perovskite (L6M7C3O). Despite this, the lattice parameter of the perovskite remains largely unaffected upon incorporation of the carbon material. On the other hand, the formation of La vacancies in the perovskite promotes the formation of M-cation species, such as manganese oxides [51]. The small peak at around 36° indicates the existence of the Mn_3O_4 oxide which has a tetragonal phase and belongs to the $I4_1/amd$ space group (PDF code: 96-101-1263).

Table 1 presents the crystallographic parameters obtained from the XRD patterns. The Rietveld refinement function of the Highscore Plus software (4.9 version) was employed to accurately estimate the concentration of LaMnO_3 and Mn_3O_4 phases in the samples. Table 1 shows that the percentage of crystalline Mn_3O_4 species, which is close to 11% in the pure oxide, increases to 14.7% in the L6M7C3O_HT sample and decreases to 9.8% in the L6M7C3O_TT sample. Hydrothermal treatment preferentially drives the formation of Mn_3O_4 species, while thermal treatment favors the formation of purer perovskite phases. The Mn_3O_4 phase, previously reported to be active for the ORR [54], could contribute to improve the electrocatalytic activity due to a potential synergistic effect between both metal oxides. The ball-milling treatment did not significantly affect the amount of Mn_3O_4 present, which remained around 11.5%—similar to the untreated perovskite (L6M7C3O sample). Next, given the importance of crystallite size in the catalytic performance, it was calculated by applying the Scherrer equation for the peaks at $22\text{--}23^\circ$ and $47\text{--}48^\circ$ [55]. The crystallite size of phases indicates that the LaMnO_3 structure has particle sizes in the range of 17–19 nm in accordance with TEM images. In contrast, the Mn_3O_4 phase exhibits a decrease in particle size when the metal oxide is mixed with carbon black by the different methods.

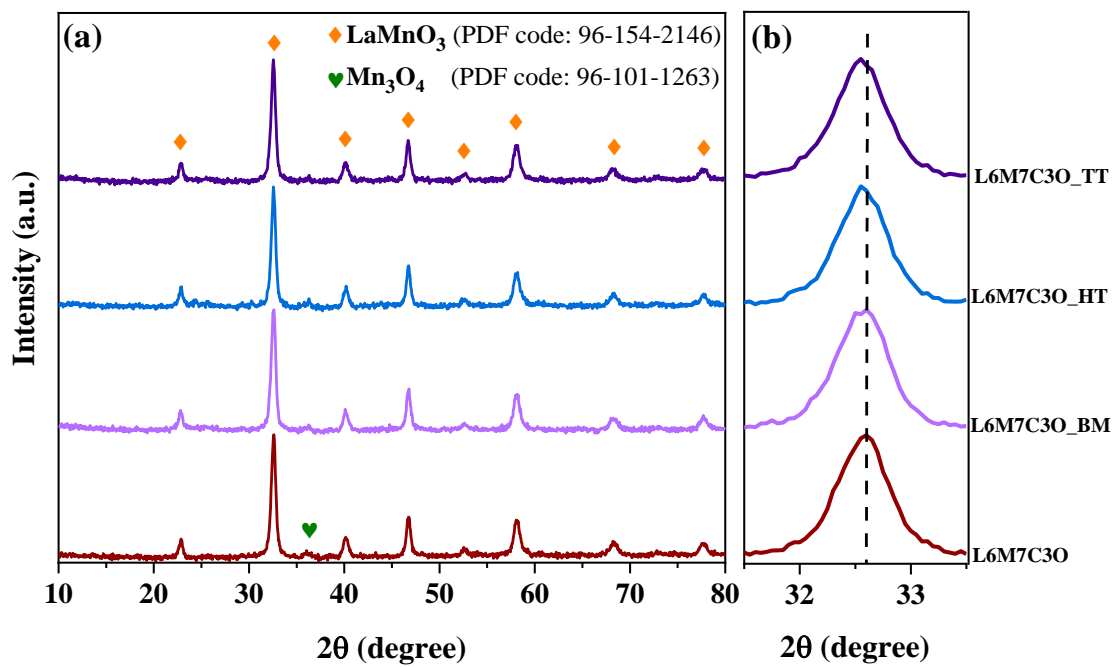


Figure 1. (a) X-ray diffraction patterns of the L6M7C3O-based materials and (b) zoom on the diffraction line at 32–33°.

Table 1. Crystal phase percentages and average crystallite size for the L6M7C3O-based materials obtained from the X-ray diffraction patterns in Figure 2.

Sample	Crystallite Phases (%)		Crystallite Size (nm)		Lattice Parameter	Lattice Volume (Å ³)
	LaMnO ₃	Mn ₃ O ₄	LaMnO ₃	Mn ₃ O ₄	LaMnO ₃	
L6M7C3O	88.7	11.3	18	20	3.886	58.697
L6M7C3O_BM	88.4	11.6	18	11	3.888	58.753
L6M7C3O_HT	85.3	14.7	19	15	3.888	58.771
L6M7C3O_TT	90.2	9.8	17	16	3.889	58.832

As the perovskite structure is the main crystallite phase, their lattice parameters were calculated using the following equations [55]:

$$d = \frac{\lambda}{2\sin \theta} \quad (1)$$

$$\frac{1}{d^2} = \frac{h^2 + k^2 + l^2}{a^2} \quad (2)$$

where d is the interplanar distance, (hkl) are the Miller indices related to the interplanar distance, and a is the lattice parameter.

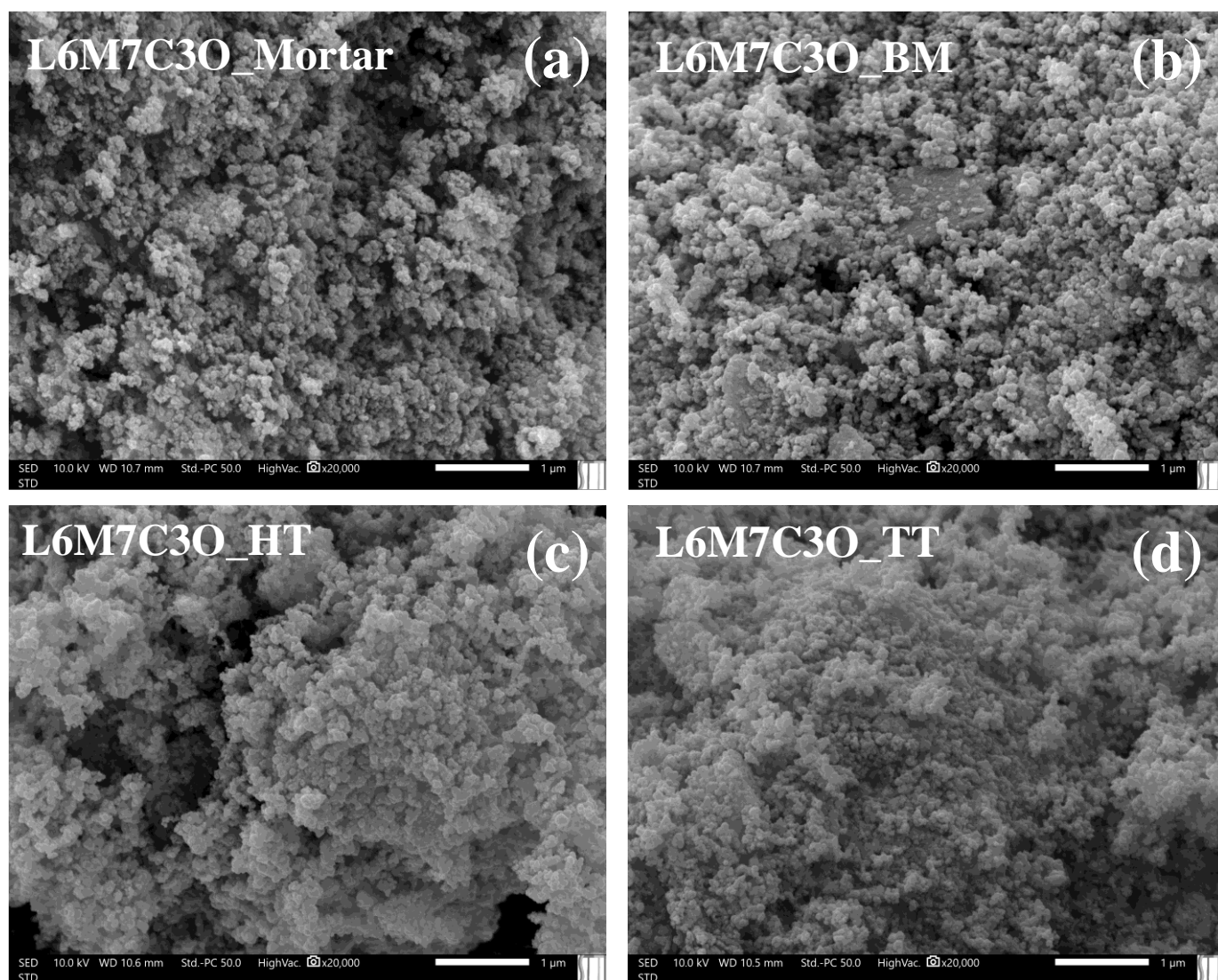


Figure 2. SEM images captured for (a) L6M7C3O_Mortar, (b) L6M7C3O_BM, (c) L6M7C3O_HT, and (d) L6M7C3O_TT. Magnification: $\times 20,000$.

3.2. Surface Structure and Composition

Porosity is desirable for electrochemical applications because it provides a larger surface-active area for the reactions, which facilitates the diffusion of reactants and products, ultimately favoring the overall electrocatalytic activity. Therefore, the surface morphology of the metal-oxide-perovskite-based materials was characterized by SEM. At a scale of $5\ \mu\text{m}$ (Figure S3), all samples exhibit spherical nanoparticle agglomerations of similar size, around $10\text{--}15\ \mu\text{m}$ in diameter. However, higher magnification reveals significant differences in particle morphology due to the mixing treatment of the components (Figure 2). The L6M7C3O_Mortar and L6M7C3O_BM samples, subjected to mechanical treatment, exhibit greater dispersion, offering a three-dimensional appearance. Conversely, samples subjected to a chemical and thermal treatment (L6M7C3O_HT and L6M7C3O_TT, respectively) display nanoparticle agglomeration, presumably due to a slight degree of sintering caused by the treatment. Therefore, these treatments seem to enhance the contact between the perovskite and Vulcan nanoparticles by causing higher compaction. Moreover, the nanoparticle size for all samples remained unchanged by the mixing treatment.

To assess the potential impact of the mixing method on the porosity of the composites (excluding the mortar-prepared sample), N_2 -adsorption isotherms were obtained at $77\ \text{K}$ (Figure S4). The isotherms displayed a type II characteristic according to the IUPAC

classification, which is indicative of non-porous materials [56]. Table S1 summarizes the textural properties derived from the N₂ isotherms. Interestingly, the L6M7C3O_HT sample exhibited the lowest BET surface area (81 m²/g), likely as a consequence of the sintering caused by the mixing method.

Previous studies reported the importance of different M-site cation oxidation states and chemisorbed oxygen species on the surface for the ORR catalytic activity [57]. Thus, XPS is a valuable technique for characterizing the surface of materials and distinguishing Mn and Co oxidation states and different oxygen species formed by the different mixing treatments. Figure 3 depicts the La 3d, Mn 2p, Co 2p, and O 1s core-level spectra for the different materials studied.

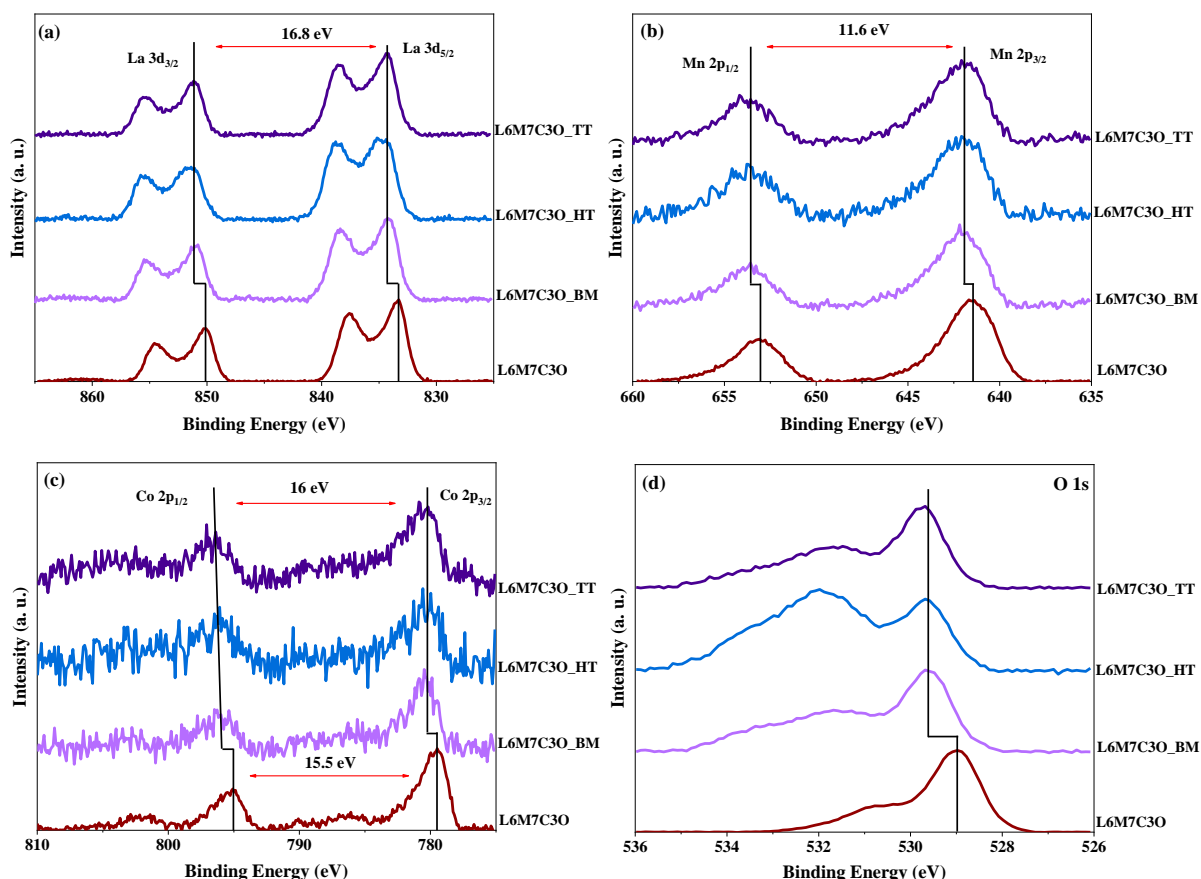


Figure 3. X-ray photoelectron signals obtained from (a) La 3d, (b) Mn 2p, (c) Co 2p, and (d) O 1s for the different composites.

The La 3d region (Figure 3a) is characterized by two well-differentiated spin–orbit components at around 834.1 eV (La 3d_{5/2}) and 851.0 eV (La 3d_{3/2}), showing a multiplet structure [53]. The main difference observed is a binding energy shift towards higher energies in the materials mixed with carbon black. This shift can be attributed to the electronegative influence of the carbon material, which alters the metallic environment through charge withdrawal. This effect, as observed in the following sections for Mn and Co cations, can be related to the ligand effect, which is one of the factors contributing to the synergistic effect observed in these materials [58]. Moreover, the separation of the La 3d_{5/2} and La 3d_{3/2} peaks in all samples corresponds to 16.8 eV, which is related to the La³⁺ species [59]. The Mn 2p spectra (Figure 3b) show two asymmetric spin–orbit signals at around 641.7 and 653.3 eV, which are attributed to Mn 2p_{3/2} and Mn 2p_{1/2}, respectively. This asymmetry suggests the presence of different Mn oxidation states, necessitating peak deconvolution for further analysis. The separation between the Mn 2p_{3/2} and Mn 2p_{1/2} peaks of 11.6 eV in all samples indicates the predominance of the

Mn³⁺ species [60]. Next, the Co 2p spectra (Figure 3c) display a pair of asymmetric spin-orbit components at 780.6 and 796.1 eV, which can be attributed to Co 2p_{3/2} and Co 2p_{1/2}, respectively. In contrast to the La and Mn spectra, these peaks exhibit variations in separation between the samples. According to the literature, a separation of 15 eV is related to Co³⁺ species, while a separation of 16 eV is related to Co²⁺ species [61]. Based on this information, the L6M7C3O sample has a mixture of Co³⁺/Co²⁺ oxidation states. Thus, the hydrothermal and thermal treatments seem to increase the peak separation, suggesting a higher presence of Co²⁺ species. The O 1s spectrum (Figure 3d) shows significant differences, and the presence of the carbon material significantly alters this region. Hence, peak deconvolution is necessary to quantify the contribution of the species in the O 1s, Mn 2p, and Co 2p spectra.

Figure 4a shows the deconvolution of the Mn 2p_{3/2} spectra, revealing three contributions at 640.5, 641.4, and 643.0 eV. Similarly, the Mn 2p_{1/2} spectra can be deconvoluted into three peaks at 652.0, 641.4, and 643.0 eV, assigned to Mn²⁺, Mn³⁺, and Mn⁴⁺, respectively [62].

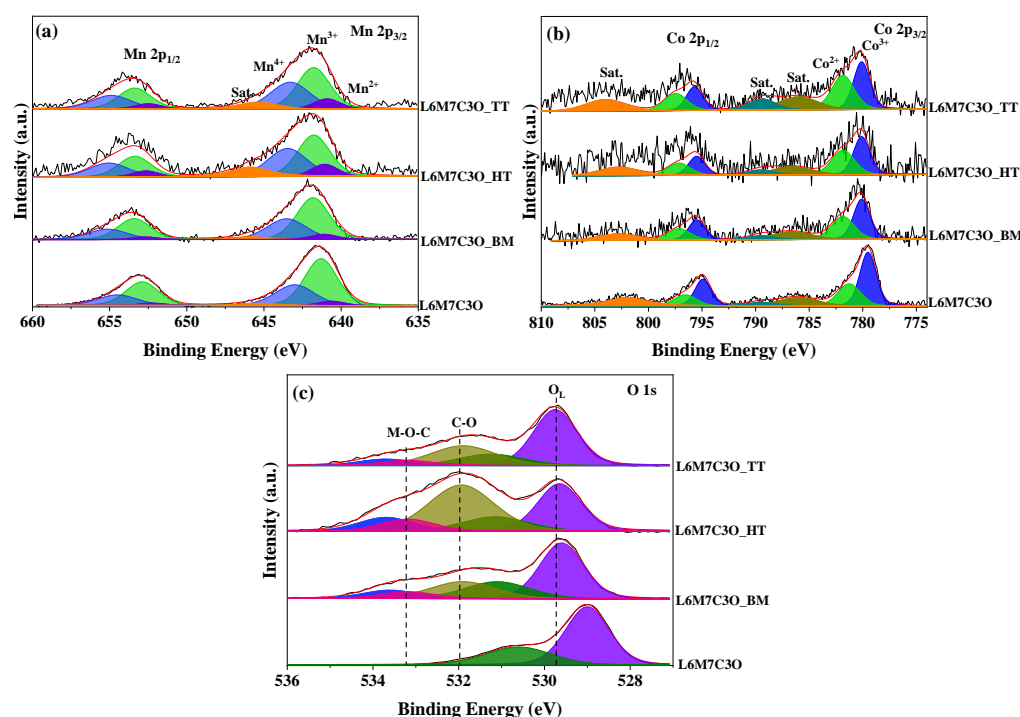


Figure 4. Deconvolution of X-ray photoelectron spectra: (a) Mn 2p, (b) Co 2p, and (c) O 1s.

An additional satellite peak at around 645.4 eV is attributed to Mn²⁺ [63]. While Mn³⁺ is the dominant oxidation state across all samples, its relative abundance varies. The L6M7C3O and L6M7C3O_BM samples mainly contain Mn³⁺ and Mn⁴⁺ species, while the chemical and thermal treatments of L6M7C3O_HT and L6M7C3O_TT samples favor the appearance of Mn²⁺. In addition, the Mn⁴⁺/Mn³⁺ ratio (Table 2) is higher in the L6M7C3O_HT and L6M7C3O_TT samples, suggesting that the formation of Mn²⁺ occurs at the expense of Mn³⁺ species.

Table 2. Experimental atomic ratios for the materials obtained from XPS technique.

Sample	Mn ⁴⁺ /Mn ³⁺	Co ³⁺ /Co ²⁺	O _C /O _L	O _{M-O-C} /O _L
L6M7C3O	0.53	1.74	0.46	-
L6M7C3O_BM	0.60	1.27	0.45	0.15
L6M7C3O_HT	0.81	0.90	0.45	0.32
L6M7C3O_TT	0.76	1.00	0.31	0.15

Furthermore, the higher presence of Mn^{4+} is expected to improve the interaction between M-site cation and oxygen species [64,65]. Additionally, its higher oxidation ability can accelerate the chemical disproportionation of HO_2^- species [64], thereby enhancing the electrocatalytic activity of the ORR.

Figure 4b shows the deconvoluted Co 2p spectra. The Co 2p_{3/2} and Co 2p_{1/2} signals are divided into two peaks assigned to Co^{3+} (at 779.8 and 794.8 eV) and Co^{2+} (at 781.2 and 796.2 eV) [66]. Table 2 shows variations in the $\text{Co}^{3+}/\text{Co}^{2+}$ ratio, with an enrichment of Co^{2+} compared to Co^{3+} in the L6M7C3O-HT and L6M7C3O-TT samples. This effect results from the increase in Mn^{4+} species on the surface, which provokes the reduction of Co^{3+} species to Co^{2+} to keep the electroneutrality on the metal surface.

The deconvolution of the O 1s spectra (Figure 4c) reveals five contributions: two assigned to the metal oxide perovskite, two assigned to the carbon material, and the fifth attributed to the interaction between both, represented by the M-O-C interaction. The peaks at 529.0 and 531.0 eV correspond to lattice oxygen species (O^{2-}) and adsorbed oxygen species (O^- , O^{2-} , or O_2^{2-}) of the perovskite, respectively. The peaks at 532.0 and 534.0 eV are associated with the C-O and C=O species of the carbon material, respectively [67]. Finally, the peak at around 533.0 eV is associated with the M-O-C species [27,68]. Additionally, differences are observed in the contribution of the C-O and M-O-C species. The hydrothermal treatment in the L6M7C3O-HT sample increases the number of C-O species in the carbon material, which potentially contributes to a stronger interaction between the carbon material and the perovskite, giving rise to a higher contribution of the M-O-C interaction [40]. Thus, the ratio between the M-O-C species and the lattice oxygen increases from 0.15 in the L6M7C3O-BM sample to 0.32 in the L6M7C3O-HT sample (Table 2). Moreover, the L6M7C3O-TT sample exhibits a more defined perovskite structure, as evidenced by XRD. This aligns with the lower ratio of oxygen from carbon to lattice oxygen among the studied samples, which can be attributed to the formation of stronger lattice oxygen bonds within the perovskite structure.

3.3. Interaction between Metal Oxide Perovskite and Carbon Material

The interaction strength between perovskite and carbon material can be a good descriptor to determine the ORR activity of a composite. Therefore, the further characterization of this interaction beyond the determination of M-O-C interactions using XPS is necessary. In this sense, the temperature-programmed reduction in H_2 (TPR- H_2) and temperature-programmed desorption (TPD) techniques were reported to be useful in providing information about the existence of this interaction [27,40,69].

TPR- H_2 is a widely used technique in catalysis to study the reducibility of catalytic species, including perovskite-type metal oxides. Significant differences in reduction behavior have been reported for perovskite-carbon composites compared to unmixed metal oxides [27,69]. Carbon material significantly influences the environment and affects the reducibility of the metal oxides due to its inherent reducing characteristic. Figure 5a shows the reduction profile of L6M7C3O perovskite without carbon for comparison purposes.

The region between 150 and 250 °C corresponds to the removal of adsorbed oxygen species. In the region between 250 and 560 °C, the reduction of Mn^{4+} to Mn^{3+} occurs, overlapping with the reduction of Co^{3+} to Co^{2+} [70,71]; these reduction processes take place in two distinct processes that are difficult to assign. The peak at around 525 °C could be ascribed to either the reduction of Co^{3+} to Co^{2+} , due to the lower proportion of Co compared to Mn, or the reduction of residual Mn^{4+} and Co^{3+} species that were not reduced at lower temperatures. Finally, a small broader peak at 650 °C related to the reduction of Co^{2+} to Co^0 and a main peak at around 750 °C associated with the reduction of Mn^{3+} to Mn^{2+} are observed [72]. The large hydrogen consumption is attributed to the Mn^{3+} species already existing in the perovskites and those resulting from the Mn^{4+} reduction. Figure 5b presents the reduction profiles of the perovskite-carbon composites. Clear differences are observed compared to pure perovskite material, namely the disappearance of the major reduction peak at 750 °C and a decrease in hydrogen consumption. The reduction by

hydrogen occurs mainly in one peak, ranging between ~ 400 and ~ 420 °C, for these samples. This means that in this region, the reduction of Mn^{4+} to Mn^{3+} and Co^{3+} to Co^{2+} occurs (similar to what occurs in the pure metal oxide perovskite). However, the disappearance of the hydrogen consumption at 750 °C indicates that the reduction of Mn^{3+} to Mn^{2+} takes place mainly through the reaction with carbon and at temperatures lower than the reaction with hydrogen.

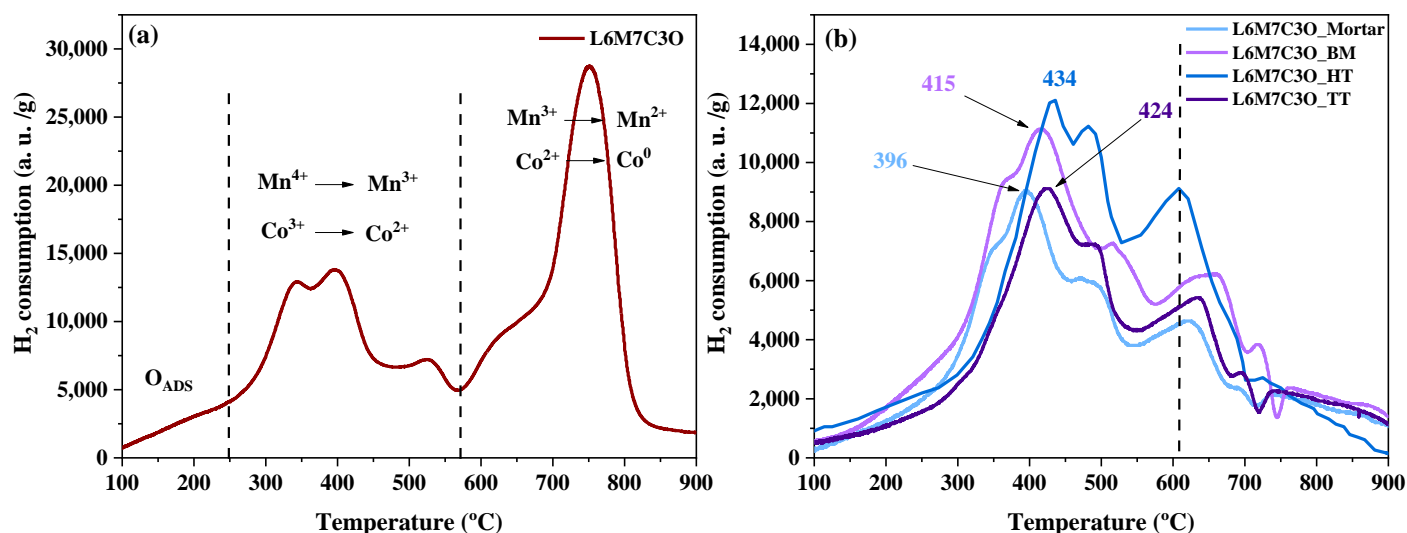


Figure 5. TPR- H_2 profile of (a) LMCO sample and (b) perovskite-carbon composites obtained by mortar mixing, ball milling, and hydrothermal and heat treatments.

The TPD technique is a highly effective analytical tool for investigating the strength and nature of the interfacial interaction in perovskite-carbon composite materials. These experiments provide valuable insights into these interactions, which have been identified as key factors in the electrocatalytic activity of the composite [14]. Figure 6 presents the TPD profiles for the different materials in which CO and CO_2 were the main desorbed species identified.

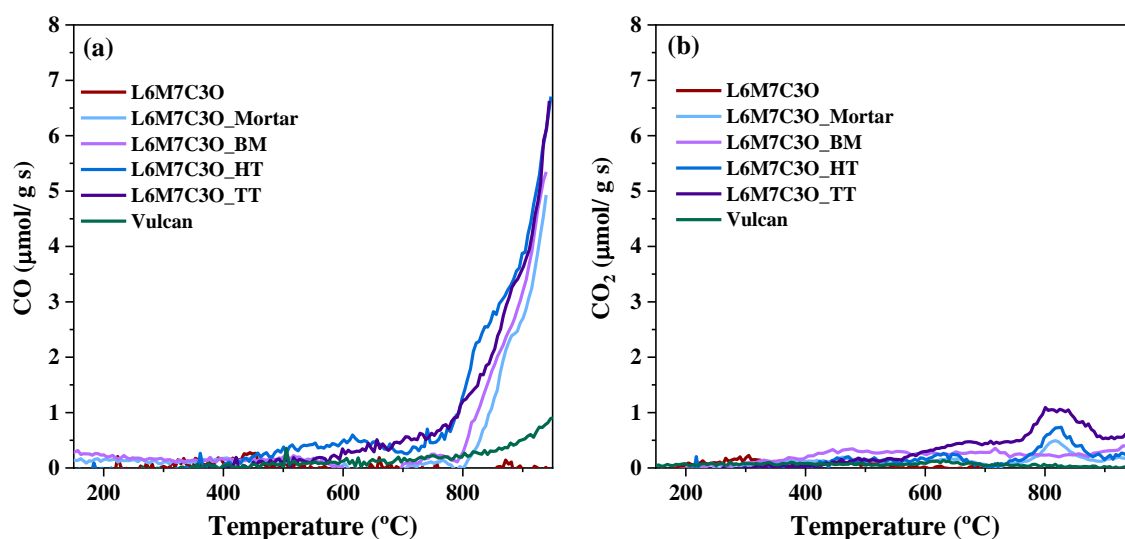


Figure 6. (a) CO and (b) CO_2 TPD profiles of perovskite-carbon composites.

The absence of O_2 desorption in the TPD experiment confirms the thermal stability of the perovskite component under the experimental temperature range, which does not result in dioxygen evolution. Moreover, the desorption of CO and CO_2 from the pure

perovskite metal oxide is negligible. In the case of Vulcan, a small desorption of CO at high temperature is observed. A quantitative determination of the desorbed species together with the experimental and theoretical oxygen amounts is presented in Table 3.

Table 3. TPD quantification of the perovskite–carbon composites. Moreover, the theoretical O concentration per gram of oxide material is shown.

Sample	$\mu\text{mol CO/g}$	$\mu\text{mol CO}_2/\text{g}$	Experimental $\mu\text{mol O/g}$	Maximum Theoretical Lattice $\mu\text{mol O/g}$
L6M7C3O	-	-	280	
L6M7C3O_Mortar	1574	833	3240	
L6M7C3O_BM	1607	823	3253	16,002
L6M7C3O_HT	1712	849	3410	
L6M7C3O_TT	1680	924	3528	
Vulcan	190	-	-	

Figure 6 shows that CO is the dominant desorbed species, with some CO₂ desorption also observed at high temperatures. The desorption of CO and CO₂ is a result of the carbothermal reduction reaction between the metal oxide perovskite and the carbon material, which occurs due to their intimate interaction at the interface [40]. It is expected that a stronger and more extensive interaction, represented by the M–O–C species, will result in higher desorption at lower temperatures. The different treatments performed on the perovskite–carbon composites result in variations in the TPD profiles of the samples (Figure 6a). Notably, the L6M7C3O and Vulcan samples separately desorb significantly lower amounts compared to the composites, indicating that the interaction between components is crucial in the observed desorption profiles. Furthermore, the total amount of desorbed oxygen due to the reaction between the carbon material and the perovskite can be calculated (Table 3). The table also includes the maximum theoretical value that corresponds to the total amount of oxygen present in the perovskite. Equation (S5) shows how this theoretical maximum value has been calculated. The results show that the highest desorption occurs in samples L6M7C3O_HT and L6M7C3O_TT, followed by L6M7C3O_Mortar and L6M7C3O_BM samples. In terms of the temperature at which CO desorption begins, it starts at around 770 °C in L6M7C3O_HT and L6M7C3O_TT samples, while in the L6M7C3O_Mortar and L6M7C3O_BM samples, it begins at around 800 °C. This demonstrates a stronger and more extensive degree of interaction between perovskite and Vulcan in the L6M7C3O_HT and L6M7C3O_TT samples, highlighting the positive effect of the hydrothermal treatment in improving the interaction of both components.

3.4. Electrochemical Characterization

The different physicochemical and morphological properties amongst the samples could suggest a different electrocatalytic activity. Cyclic voltammetry tests were performed in a N₂-saturated 0.1 M KOH solution and the results are depicted in Figure 7a.

The main difference observed is the lower electrochemical capacitance and conductivity of the pure metal oxide perovskite sample compared to the perovskite–carbon composites. This is evidenced by the tilted voltammogram of the pure perovskite, which often indicates a high ohmic resistance that overlaps with the recorded current densities. The perovskite–carbon composites display two faradaic processes related to the Mn²⁺/Mn³⁺ redox process occurring at around 0.7 V and a peak around 1.0 V related to the formation of MnOOH species [73,74]. No significant differences are observed in the voltammograms of the composites.

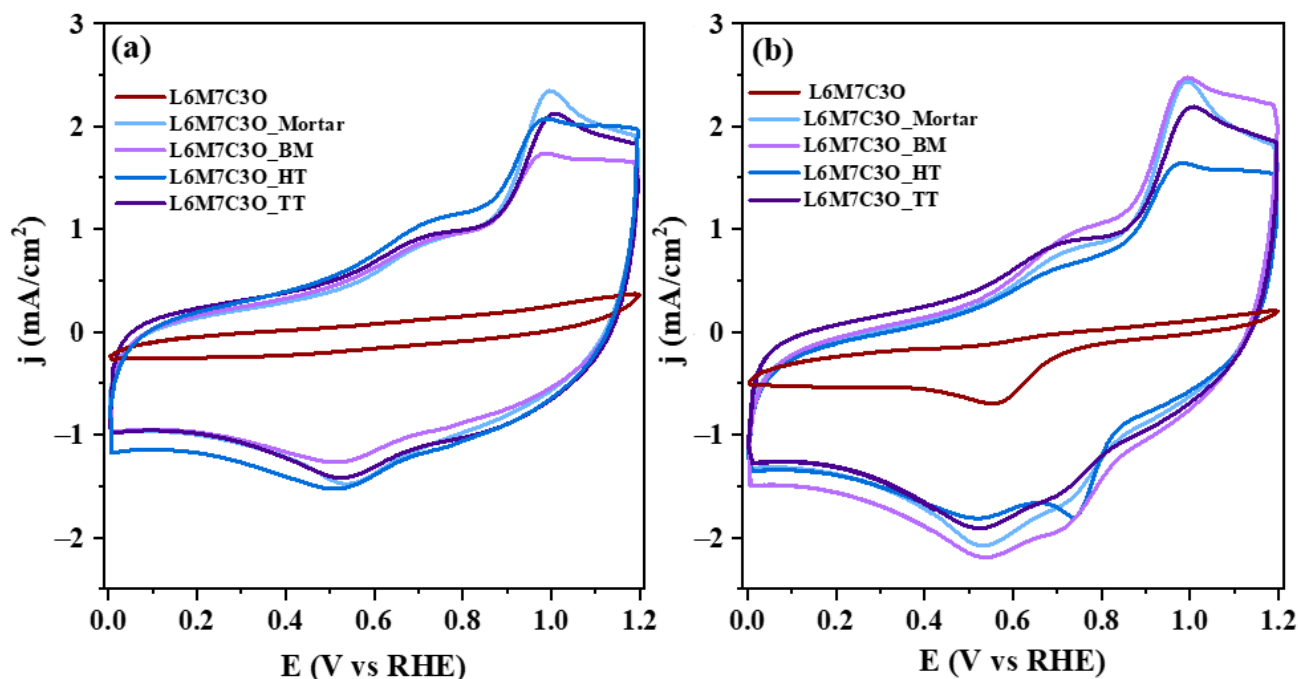


Figure 7. Cyclic voltammograms for the different perovskite–carbon composites in 0.1 M KOH solution saturated with either (a) N_2 or (b) O_2 . Scan rate: 50 mV/s.

As explained in the introduction, combining cations at the M-site and A-site can be beneficial in increasing the surface concentration of active sites in metal oxide perovskites. For this reason, Table 4 compares the ORR parameters of the L6M7C3O_Mortar material prepared in this study with samples with different compositions previously published and prepared using a similar mortar-based approach ($LaMn_{0.7}Co_{0.3}O_3$ _Mortar [27] and $La_{0.6}MnO_z$ _Mortar [51]). Figure S5 compares the LSV obtained during the ORR for all samples mixed with carbon material using mortar (L6M7C3O_Mortar, $LaMn_{0.7}Co_{0.3}O_3$ _Mortar, and $La_{0.6}MnO_z$ _Mortar). The results demonstrate that the L6M7C3O_Mortar prepared in this study exhibits better electrocatalytic behavior, evidenced by its lower Tafel slope and higher $E_{1/2}$ value. The enhanced electrocatalytic activity of the L6M7C3O_Mortar sample is then a consequence of the optimized composition of La and Co species. For this reason, this specific composition for the metal oxide perovskite is the one that has been used in the different preparation methods described in this study. The observed improvement with this specific composition can be related to some combined effects, such as the generation of charge compensation mechanisms due to differences in the oxidation states of the cations; the occurrence of synergy between the two cations; the induction of altered (and more favorable) arrangements in the resulting composite, like porous structures that facilitate the diffusion of electrolytes or oxygen into the perovskite material; or the formation of additional metal redox pairs [53,75]. Figure 8 shows the electrochemical activity towards the ORR evaluated in an RRDE in a 0.1 M KOH electrolyte for the samples in which the carbon material has been introduced through different approaches.

Table 4 displays the main electrochemical parameters of the ORR. The L6M7C3O sample presents an E_{onset} of 0.76 V at -0.10 mA/cm², showing the least favorable result in the series.

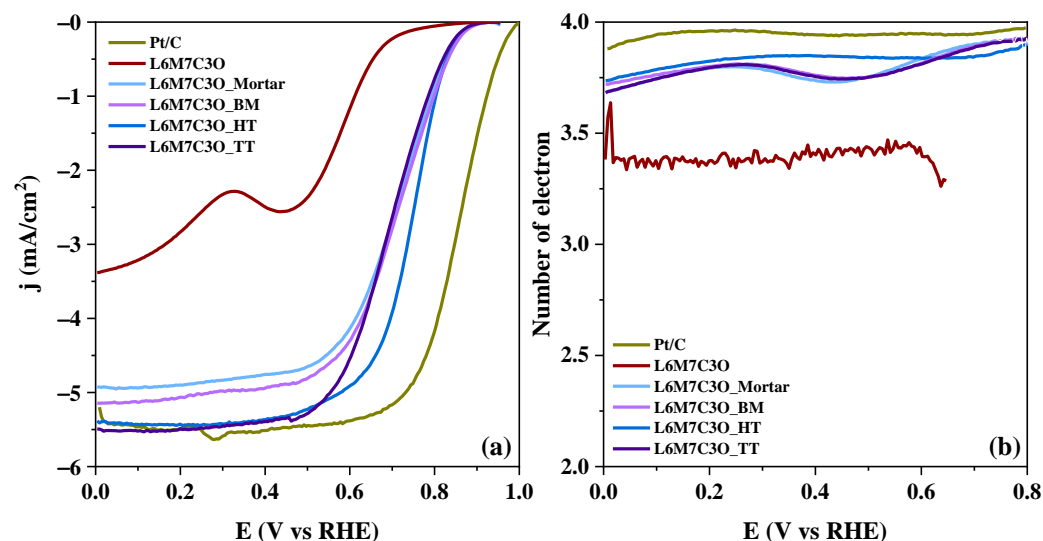


Figure 8. (a) Linear sweep voltammograms for the different composites in 0.1 M KOH solution saturated with O_2 at 1600 rpm, $v = 5$ mV/s; (b) number of electrons transferred in ORR using the current measured at the ring electrode.

Table 4. Electrochemical parameters obtained for ORR at the different samples.

Sample	E_{onset}/V (at -0.10 mA/cm 2)	n_{e-} (at 0.4)	$j_{lim}/\text{mA}/\text{cm}^2$ (at 0.4 V)	$E_{1/2}$ (V)	Tafel Slope/mV/dec
L6M7C3O	0.76	3.40	−2.49	–	−169
L6M7C3O_Mortar	0.87	3.74	−4.76	0.71	−75
L6M7C3O_BM	0.88	3.76	−4.94	0.72	−63
L6M7C3O_HT	0.87	3.85	−5.36	0.75	−62
L6M7C3O_TT	0.87	3.76	−5.40	0.70	−66
Pt/Carbon	0.98	3.96	−5.51	0.86	−60
LaMn $_{0.7}$ Co $_{0.3}$ O $_3$ _Mortar	0.84	3.78	−4.82	0.66	−81
La $_{0.6}$ MnO $_z$ _Mortar	0.87	3.81	−4.78	0.69	−90

It can be observed that the electrocatalytic activity improves for the samples with carbon material. Moreover, the results demonstrate a similar performance among the samples mixed with carbon material, although differences are detected in terms of the half-wave potential and limiting current density. The half-wave potential ($E_{1/2}$) is a widely accepted indicator for evaluating ORR performance, and higher values of $E_{1/2}$ correspond to a lower overpotential to the reaction [76]. Thus, the sample that shows the higher ORR activity is the L6M7C3O_HT sample with the highest $E_{1/2}$ value of 0.75 V. Concerning the limiting current density (j_{lim}), the samples subjected to chemical treatment (L6M7C3O_HT and L6M7C3O_TT) are the ones that present the largest current density, −5.36 and −5.40 mA/cm 2 at 0.4 V, respectively.

The Tafel analysis is an effective tool for studying electron rate-determining processes. In general, small Tafel values imply better ORR activities [77]. As shown in Table 4 and Figure S6, the Tafel slopes for the samples decrease when carbon material is present. In all cases, the results are close to 60 mV/dec, showing that the carbon material influences the electron transfer kinetics.

The number of electrons transferred in the ORR can be observed in Figure 8b. All perovskite–carbon composites exhibit a nearly four-electron transfer pathway, with the L6M7C3O_HT sample showing the highest value of electrons transferred at 0.4 V. However, the limiting current obtained for this sample shows that this electrocatalyst can be an alternative to commercial Pt/C for this reaction.

Then, the superior electrocatalytic activity observed in the L6M7C3O_HT sample compared to the others can be attributed to its physicochemical and morphological properties. First, a higher presence of the electroactive compound Mn_3O_4 was detected in the L6M7C3O_HT sample, which likely contributes to an improvement in electrocatalytic activity. Second, the extent of interaction between the perovskite and the carbon material is among the highest. Moreover, the positive synergistic effect between both metal oxides cannot be ruled out.

XPS analysis revealed a higher presence of the M-O-C species in the L6M7C3O_HT sample, indicating the strongest interfacial interaction. Additionally, TPD showed the highest amount of desorbed oxygen for the L6M7C3O_HT sample, further demonstrating a more intimate and extensive contact between the components. The L6M7C3O_TT sample also showed a similar amount of oxygen desorbed, highlighting the positive influence of both hydrothermal and thermal treatments in improving the interaction between perovskite and carbon material. On the other hand, surface morphology studies have revealed differences in the morphology of perovskite and carbon materials, with improved properties observed in the L6M7C3O_HT and L6M7C3O_TT samples.

Furthermore, XPS analysis revealed the significant influence of the carbon material in modifying the electronic environment of the cations, shifting the peaks towards higher binding energies. The mixing method was also found to affect the oxidation state distribution of the cations. Thus, the greater performance of the L6M7C3O_HT sample might also be related to its higher concentration of Mn^{4+} species, which benefits the interaction between active sites and oxygen species and the hydroperoxide disproportionation reaction.

4. Zn–Air Battery

The L6M7C3O_HT sample has been studied using a ZAB system (Figure S7). Its performance is compared to that of the L6M7C3O_BM sample, which exhibits similar ORR results. The L6M7C3O_BM sample was chosen as a reference due to its significantly simpler synthesis process, which could facilitate large-scale production.

The electrochemical performance of the synthesized materials was further analyzed using a ZAB under operating conditions.

In this setup, a zinc plate was used as the anode, while the air cathode (2.8 cm^2 of geometrical area) comprised perovskite–carbon composites on carbon paper (gas diffusion layer) with a loading density of 1.3 mg/cm^2 . The electrolyte used was a mixture of 6.0 M KOH and 0.2 M $\text{Zn}(\text{O}_2\text{CCH}_3)_2 \cdot 2\text{H}_2\text{O}$ solution. A battery assembled with commercial Pt/C served as a reference for comparison. Figure 9a depicts the discharge polarization curve, where the L6M7C3O_BM sample exhibits a peak power density of 46.2 mW/cm^2 at a current density of 78.0 mA/cm^2 and the L6M7C3O_HT sample shows a maximum power density peak at 43.9 mW/cm^2 at 77.2 mA/cm^2 ; these values do not exceed the performance of the commercial Pt/C catalyst, which achieves a maximum power of 78.4 mW/cm^2 at a current density of 124.6 mA/cm^2 . However, differences are observed between the samples, with the L6M7C3O_BM sample exhibiting a slightly better performance at higher current densities. The sample developed in this work shows stable voltage values when subjected to different discharge current densities (2, 5, 20, 50, and back to 2 mA/cm^2) (Figure 9b), also displaying good reversibility after operating at high current densities. Figure 9c shows the galvanostatic capacity curves at 5 and 10 mA/cm^2 for L6M7C3O_BM (790 and 748 mAh/g_{Zn} , respectively) and L6M7C3O_HT (800 and 768 mAh/g_{Zn}). These values are higher than those obtained for Pt/C at 5 and 10 mA/cm^2 (741 and 738 mAh/g_{Zn} , respectively (Figure S8)).

It has been demonstrated that both samples are capable of acting as an air electrode in primary Zn–air batteries. While their performance does not surpass that of the high-activity commercial Pt/C catalyst, the focus of this work was on developing cost-effective and easily scalable electrocatalysts. Table S2 highlights the significant cost advantage of the perovskite materials used in this study (ranging from 1.55 to 25.34 USD/kg) compared to Pt (26,696.82 USD/kg), emphasizing the low-cost and simple synthesis procedures

employed. Interestingly, the performance of the L6M7C3O_BM sample is very similar to that of L6M7C3O_HT. Considering its simpler synthesis process (ball milling eliminates the need for thermal treatment), we believe that the L6M7C3O_BM sample is the most promising candidate for further development.

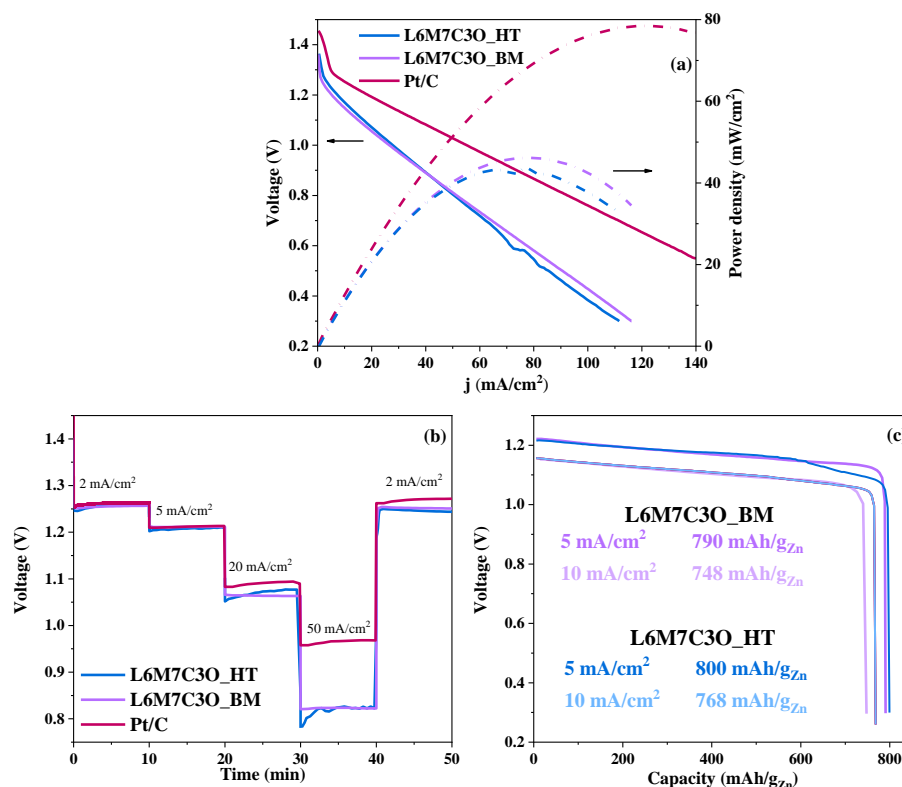


Figure 9. (a) Discharge polarization curves and power density for L6M7C3O_BM and Pt/C. (b) Discharge curves from 2 to 50 mA/cm². (c) Galvanostatic discharge curves at 5 and 10 mA/cm² for L6M7C3O_BM and L6M7C3O_HT samples.

5. Conclusions

It has been demonstrated that there is an effect on the electrocatalytic activity towards the ORR depending on the mixing method used between perovskite-type metal oxides and the carbon material Vulcan. The L6M7C3O_HT sample exhibited superior ORR performance compared to the others, highlighting the effectiveness of hydrothermal treatment in improving the interaction between the carbon material and the perovskite. First, XPS analysis identified a greater abundance of the M-O-C species in this material; this suggests the formation of the strongest interfacial interaction in this sample. Furthermore, TPD measurements revealed the highest desorption of oxygen for the L6M7C3O_HT sample, confirming a more intimate and extensive contact between the constituent elements. The enhancement in the interaction has led to improved electrocatalytic activity. However, electrocatalytic activity is not the only factor to consider when synthesizing electrocatalysts. This study has also highlighted the importance of cost-effective and scalable synthesis methods. The L6M7C3O_BM sample is preferable due to its simpler synthesis process (ball milling) while maintaining similar electrocatalytic activity to the L6M7C3O_HT sample. Furthermore, its performance in a primary Zn–air battery has been demonstrated. Therefore, this study proposes the use of the ball mill as a mixing method for perovskite-type metal oxides and Vulcan. Based on the findings of this work, a future line of research could be the one-step hydrothermal synthesis of perovskite–carbon composites, with the optimization of conditions such as temperature and time. This would involve synthesizing the perovskite using the hydrothermal method in the presence of the carbon material. This

approach would take advantage of the improved interaction provided by the hydrothermal method, while also enhancing the simplicity of the synthesis.

Supplementary Materials: The following supporting information can be downloaded at <https://www.mdpi.com/article/10.3390/ma17102309/s1>, References [55,56,78] are cited in the supplementary materials; Figure S1: L6M7C3O perovskite TEM image; Figure S2: TEM images of the (A) L6M7C3O_Mortar, (B) L6M7C3O_BM, (C) L6M7C3O_HT and (D) L6M7C3O_TT; Figure S3: SEM images for (a) L6M7C3O_Mortar, (b) L6M7C3O_BM, (c) L6M7C3O_HT and (d) L6M7C3O_TT. Magnification: $\times 5000$; Figure S4: Nitrogen adsorption isotherms of the composite materials; Table S1: Textural parameters obtained from the N_2 isotherms; Figure S5: (a) RRDE linear sweep voltammograms for the comparison of the sample of this work (L6M7C3O_Mortar) with samples from previous works in 0.1 M KOH solution saturated with O_2 at 1600 rpm, $v = 5$ mV/s; (b) Number of electrons transferred in ORR at increasing potential as obtained from Equation (S3) by using the current measured at the ring electrode; Figure S6: ORR Tafel slopes; Figure S7: Image of the battery system used in this work; Figure S8: Galvanostatic discharge curve at 5 and 10 mA/cm² for Pt/C commercial catalysts; Table S2: Comparison of the prices of the metals used in this study and their comparison with Pt.

Author Contributions: Methodology, M.G.-R., J.X.F.-L., D.C.-A. and E.M.; Formal analysis, M.G.-R. and J.X.F.-L.; Investigation, M.G.-R., J.X.F.-L. and D.C.-A.; Resources, D.C.-A. and E.M.; Writing—original draft, M.G.-R. and J.X.F.-L.; Writing—review & editing, D.C.-A. and E.M.; Supervision, D.C.-A. and E.M.; Funding acquisition, E.M. All authors have read and agreed to the published version of the manuscript.

Funding: The authors would like to thank the PID2022-137566OB-I00 project funded by MCIN/AEI/10.13039/501100011033 and by “ERDF A way of making Europe”, by the “European Union”. Mario García-Rodríguez thanks the Ministerio de Universidades for the FPU20-01746 grant. And the APC was funded by the University of Alicante.

Institutional Review Board Statement: Not applicable.

Informed Consent Statement: Not applicable.

Data Availability Statement: Data are contained within the article and Supplementary Materials.

Conflicts of Interest: The authors declare that they have no known competing financial interests or personal relationships that could have appeared to influence the work reported in this paper.

References

- Montoya, J.H.; Seitz, L.C.; Chakthranont, P.; Vojvodac, A.; Jaramillo, T.F.; Nørskov, J.K. Materials for solar fuels and chemicals. *Nat. Mater.* **2017**, *16*, 70–81. [\[CrossRef\]](#) [\[PubMed\]](#)
- Wei, C.; Rao, R.R.; Peng, J.; Huang, B.; Stephens, I.E.L.; Risch, M.; Xu, Z.J.; Shao-Horn, Y. Recommended Practices and Benchmark Activity for Hydrogen and Oxygen Electrocatalysis in Water Splitting and Fuel Cells. *Adv. Mater.* **2019**, *31*, 1806296. [\[CrossRef\]](#) [\[PubMed\]](#)
- Xiao, F.; Wang, Y.; Wu, Z.; Chen, G.; Yang, F.; Zhu, S.; Siddharth, K.; Kong, Z.; Lu, A.; Li, J.; et al. Recent Advances in Electrocatalysts for Proton Exchange Membrane Fuel Cells and Alkaline Membrane Fuel Cells. *Adv. Mater.* **2021**, *33*, 2006292. [\[CrossRef\]](#) [\[PubMed\]](#)
- Chen, X.; Jia, Y.; Shi, Z.; Le, Q.; Li, J.; Zhang, M.; Liu, M.; Atrens, A. Understanding the discharge behavior of an ultra-high-purity Mg anode for Mg–air primary batteries. *J. Mater. Chem. A* **2021**, *9*, 21387–21401. [\[CrossRef\]](#)
- Leong, K.W.; Wang, Y.; Ni, M.; Pan, W.; Luo, S.; Leung, D.Y.C. Rechargeable Zn–air batteries: Recent trends and future perspectives. *Renew. Sustain. Energy Rev.* **2022**, *154*, 111771. [\[CrossRef\]](#)
- Fu, J.; Liang, R.; Liu, G.; Yu, A.; Bai, Z.; Yang, L.; Chen, Z. Recent Progress in Electrically Rechargeable Zinc–Air Batteries. *Adv. Mater.* **2019**, *31*, 1805230. [\[CrossRef\]](#)
- Wang, Q.; Kaushik, S.; Xiao, X.; Xu, Q. Sustainable zinc–air battery chemistry: Advances, challenges and prospects. *Chem. Soc. Rev.* **2023**, *52*, 6139–6190. [\[CrossRef\]](#) [\[PubMed\]](#)
- Zhang, Y.-L.; Goh, K.; Zhao, L.; Sui, X.-L.; Gong, X.-F.; Cai, J.-J.; Zhou, Q.-Y.; Zhang, H.-D.; Li, L.; Kong, F.-R.; et al. Advanced non-noble materials in bifunctional catalysts for ORR and OER toward aqueous metal–air batteries. *Nanoscale* **2020**, *12*, 21534–21559. [\[CrossRef\]](#)
- Xu, X.; Pan, Y.; Zhong, Y.; Ran, R.; Shao, Z. Ruddlesden–Popper perovskites in electrocatalysis. *Mater. Horiz.* **2020**, *7*, 2519–2565. [\[CrossRef\]](#)

10. Flores-Lasluisa, J.X.; García-Rodríguez, M.; Cazorla-Amorós, D.; Morallón, E. In-situ synthesis of encapsulated N-doped carbon metal oxide nanostructures for Zn-air battery applications. *Carbon* **2024**, *225*, 119147. [\[CrossRef\]](#)
11. Retuerto, M.; Calle-Vallejo, F.; Pascual, L.; Lumbeeck, G.; Fernandez-Diaz, M.T.; Croft, M.; Gopalakrishnan, J.; Peña, M.A.; Hadermann, J.; Greenblatt, M.; et al. La_{1.5}Sr_{0.5}NiMn_{0.5}Ru_{0.5}O₆ Double Perovskite with Enhanced ORR/OER Bifunctional Catalytic Activity. *ACS Appl. Mater. Interfaces* **2019**, *11*, 21454–21464. [\[CrossRef\]](#) [\[PubMed\]](#)
12. Abdelghafar, F.; Xu, X.; Jiang, S.P.; Shao, Z. Perovskite for Electrocatalytic Oxygen Evolution at Elevated Temperatures. *ChemSusChem* **2024**, e202301534. [\[CrossRef\]](#) [\[PubMed\]](#)
13. Wang, C.; Zeng, L.; Guo, W.; Gong, C.; Yang, J. Enhancing oxygen and hydrogen evolution activities of perovskite oxide LaCoO₃ via effective doping of platinum. *RSC Adv.* **2019**, *9*, 35646–35654. [\[CrossRef\]](#) [\[PubMed\]](#)
14. Zhu, Y.; Zhou, W.; Shao, Z. Perovskite/Carbon Composites: Applications in Oxygen Electrocatalysis. *Small* **2017**, *13*, 1603793. [\[CrossRef\]](#) [\[PubMed\]](#)
15. Liu, D.; Zhou, P.; Bai, H.; Ai, H.; Du, X.; Chen, M.; Liu, D.; Ip, W.F.; Lo, K.H.; Kwok, C.T.; et al. Development of Perovskite Oxide-Based Electrocatalysts for Oxygen Evolution Reaction. *Small* **2021**, *17*, 2101605. [\[CrossRef\]](#) [\[PubMed\]](#)
16. Flores-Lasluisa, J.X.; Huerta, F.; Cazorla-Amorós, D.; Morallón, E. Transition metal oxides with perovskite and spinel structures for electrochemical energy production applications. *Environ. Res.* **2022**, *214*, 113731. [\[CrossRef\]](#)
17. Li, T.; Liu, J.; Jin, X.; Wang, F.; Song, Y. Composition-dependent electro-catalytic activities of covalent carbon-LaMnO₃ hybrids as synergistic catalysts for oxygen reduction reaction. *Electrochim. Acta* **2016**, *198*, 115–126. [\[CrossRef\]](#)
18. García-Rodríguez, M.; Cazorla-Amorós, D.; Morallón, E. Enhanced lanthanum-stabilized low crystallinity metal oxide electrocatalysts with superior activity for oxygen reactions. *Electrochim. Acta* **2024**, *479*, 143858. [\[CrossRef\]](#)
19. Kéranguéven, G.; Bouillet, C.; Papaefthymiou, V.; Simonov, P.A.; Savinova, E.R. How key characteristics of carbon materials influence the ORR activity of LaMnO₃- and Mn₃O₄-carbon composites prepared by in situ autocombustion method. *Electrochim. Acta* **2020**, *353*, 136557. [\[CrossRef\]](#)
20. Maillard, F.; Simonov, P.A.; Savinova, E.R. Carbon Materials as Supports for Fuel Cell Electrocatalysts. In *Carbon Materials for Catalysis*; John Wiley & Sons, Inc.: Hoboken, NJ, USA, 2008; pp. 429–480. [\[CrossRef\]](#)
21. Beall, C.E.; Fabbri, E.; Schmidt, T.J. Perovskite Oxide Based Electrodes for the Oxygen Reduction and Evolution Reactions: The Underlying Mechanism. *ACS Catal.* **2021**, *11*, 3094–3114. [\[CrossRef\]](#)
22. Hermann, V.; Dutriat, D.; Müller, S.; Comninellis, C. Mechanistic studies of oxygen reduction at La_{0.6}Ca_{0.4}CoO₃-activated carbon electrodes in a channel flow cell. *Electrochim. Acta* **2000**, *46*, 365–372. [\[CrossRef\]](#)
23. Li, X.; Qu, W.; Zhang, J.; Wang, H. Electrocatalytic Activities of La_{0.6}Ca_{0.4}CoO₃ and La_{0.6}Ca_{0.4}CoO₃-Carbon Composites Toward the Oxygen Reduction Reaction in Concentrated Alkaline Electrolytes. *J. Electrochem. Soc.* **2011**, *158*, A597. [\[CrossRef\]](#)
24. Suntivich, J.; Gasteiger, H.A.; Yabuuchi, N.; Nakanishi, H.; Goodenough, J.B.; Shao-Horn, Y. Design principles for oxygen-reduction activity on perovskite oxide catalysts for fuel cells and metal–air batteries. *Nat. Chem.* **2011**, *3*, 546–550. [\[CrossRef\]](#)
25. Du, J.; Zhang, T.; Cheng, F.; Chu, W.; Wu, Z.; Chen, J. Nonstoichiometric Perovskite CaMnO_{3–δ} for Oxygen Electrocatalysis with High Activity. *Inorg. Chem.* **2014**, *53*, 9106–9114. [\[CrossRef\]](#) [\[PubMed\]](#)
26. Zhang, J.; Zhao, Y.; Zhao, X.; Liu, Z.; Chen, W. Porous Perovskite LaNiO₃ Nanocubes as Cathode Catalysts for Li–O₂ Batteries with Low Charge Potential. *Sci. Rep.* **2014**, *4*, 6005. [\[CrossRef\]](#)
27. Flores-Lasluisa, J.X.; Huerta, F.; Cazorla-Amorós, D.; Morallón, E. Carbon Material and Cobalt-Substitution Effects in the Electrochemical Behavior of LaMnO₃ for ORR and OER. *Nanomaterials* **2020**, *10*, 2394. [\[CrossRef\]](#) [\[PubMed\]](#)
28. Jin, C.; Yang, Z.; Cao, X.; Lu, F.; Yang, R. A novel bifunctional catalyst of Ba_{0.9}Co_{0.5}Fe_{0.4}Nb_{0.1}O_{3–δ} perovskite for lithium–air battery. *Int. J. Hydrogen Energy* **2014**, *39*, 2526–2530. [\[CrossRef\]](#)
29. Jin, C.; Cao, X.; Lu, F.; Yang, Z.; Yang, R. Electrochemical study of Ba_{0.5}Sr_{0.5}Co_{0.8}Fe_{0.2}O₃ perovskite as bifunctional catalyst in alkaline media. *Int. J. Hydrogen Energy* **2013**, *38*, 10389–10393. [\[CrossRef\]](#)
30. Oh, M.Y.; Lee, J.J.; Park, H.S.; Kim, T.-Y.; Lee, Y.-S.; Vanchiappan, A.; Nahm, K.S. Efficient bifunctional catalytic activity of nanoscopic Pd-decorated La_{0.6}Sr_{0.4}CoO₃- perovskite toward Li–O₂ battery, oxygen reduction, and oxygen evolution reactions. *J. Ind. Eng. Chem.* **2019**, *80*, 686–695. [\[CrossRef\]](#)
31. Wang, Z.; Zou, L.; Guo, S.; Sun, M.; Chen, Y.; Chi, B.; Pu, J.; Li, J. Porous double-doped perovskite La_{0.6}Ca_{0.4}Fe_{0.8}Ni_{0.2}O₃ nanotubes as highly efficient bifunctional catalysts for lithium–oxygen batteries. *J. Power Sources* **2020**, *468*, 228362. [\[CrossRef\]](#)
32. Islam, M.; Jeong, M.-G.; Ghani, F.; Jung, H.-G. Micro Emulsion Synthesis of LaCoO₃ Nanoparticles and their Electrochemical Catalytic Activity. *J. Electrochem. Sci. Technol.* **2015**, *6*, 121–130. [\[CrossRef\]](#)
33. Alexander, C.T.; Abakumov, A.M.; Forslund, R.P.; Johnston, K.P.; Stevenson, K.J. Role of the Carbon Support on the Oxygen Reduction and Evolution Activities in LaNiO₃ Composite Electrodes in Alkaline Solution. *ACS Appl. Energy Mater.* **2018**, *1*, 1549–1558. [\[CrossRef\]](#)
34. Zhang, Y.; Wang, Y.; Huang, J.; Han, C.; Zang, J. Mn₃O₄ nanosheets coated on carbon nanotubes as efficient electrocatalysts for oxygen reduction reaction. *Int. J. Hydrogen Energy* **2020**, *45*, 6529–6537. [\[CrossRef\]](#)
35. Rebekah, A.; Ashok Kumar, E.; Viswanathan, C.; Ponpandian, N. Effect of cation substitution in MnCo₂O₄ spinel anchored over rGO for enhancing the electrocatalytic activity towards oxygen evolution reaction (OER). *Int. J. Hydrogen Energy* **2020**, *45*, 6391–6403. [\[CrossRef\]](#)
36. Zhuang, S.; Wang, Z.; He, J.; Jia, D.; Wang, Q.; Lu, M.; Tu, F. Perovskite La_{0.5}Ca_{0.5}CoO_{3–δ} nanocrystals on graphene as a synergistic catalyst for rechargeable zinc–air batteries. *Sustain. Mater. Technol.* **2021**, *29*, e00282. [\[CrossRef\]](#)

37. Hu, J.; Shi, Z.; Su, C.; Lu, B.; Shao, Z.; Huang, H. Anchoring perovskite LaMnO₃ nanoparticles on biomass-derived N, P co-doped porous carbon for efficient oxygen reduction. *Electrochim. Acta* **2018**, *274*, 40–48. [\[CrossRef\]](#)
38. Liu, W.; Rao, D.; Bao, J.; Xu, L.; Lei, Y.; Li, H. Strong coupled spinel oxide with N-rGO for high-efficiency ORR/OER bifunctional electrocatalyst of Zn-air batteries. *J. Energy Chem.* **2021**, *57*, 428–435. [\[CrossRef\]](#)
39. Ge, X.; Goh, F.W.T.; Li, B.; Hor, T.S.A.; Zhang, J.; Xiao, P.; Wang, X.; Zong, Y.; Liu, Z. Efficient and durable oxygen reduction and evolution of a hydrothermally synthesized La(Co_{0.55}Mn_{0.45})_{0.99}O_{3-δ} nanorod/graphene hybrid in alkaline media. *Nanoscale* **2015**, *7*, 9046–9054. [\[CrossRef\]](#) [\[PubMed\]](#)
40. García-Rodríguez, M.; Flores-Lasluisa, J.X.; Cazorla-Amorós, D.; Morallón, E. Metal oxide Perovskite-Carbon composites as electrocatalysts for zinc-air batteries. Optimization of ball-milling mixing parameters. *J. Colloid Interface Sci.* **2023**, *630*, 269–280. [\[CrossRef\]](#)
41. Wang, Z.; You, Y.; Yuan, J.; Yin, Y.-X.; Li, Y.-T.; Xin, S.; Zhang, D. Nickel-Doped La_{0.8}Sr_{0.2}Mn_{1-x}Ni_xO₃ Nanoparticles Containing Abundant Oxygen Vacancies as an Optimized Bifunctional Catalyst for Oxygen Cathode in Rechargeable Lithium–Air Batteries. *ACS Appl. Mater. Interfaces* **2016**, *8*, 6520–6528. [\[CrossRef\]](#)
42. Zhu, Y.; Zhou, W.; Yu, J.; Chen, Y.; Liu, M.; Shao, Z. Enhancing Electrocatalytic Activity of Perovskite Oxides by Tuning Cation Deficiency for Oxygen Reduction and Evolution Reactions. *Chem. Mater.* **2016**, *28*, 1691–1697. [\[CrossRef\]](#)
43. Zhu, Y.; Zhou, W.; Sunarso, J.; Zhong, Y.; Shao, Z. Phosphorus-Doped Perovskite Oxide as Highly Efficient Water Oxidation Electrocatalyst in Alkaline Solution. *Adv. Funct. Mater.* **2016**, *26*, 5862–5872. [\[CrossRef\]](#)
44. Hu, J.; Liu, Q.; Shi, Z.; Zhang, L.; Huang, H. LaNiO₃-nanorod/graphene composite as an efficient bi-functional catalyst for zinc–air batteries. *RSC Adv.* **2016**, *6*, 86386–86394. [\[CrossRef\]](#)
45. Liu, Z.; Cheng, H.; Li, N.; Ma, T.Y.; Su, Y. ZnCo₂O₄ Quantum Dots Anchored on Nitrogen-Doped Carbon Nanotubes as Reversible Oxygen Reduction/Evolution Electrocatalysts. *Adv. Mater.* **2016**, *28*, 3777–3784. [\[CrossRef\]](#)
46. Prabu, M.; Ramakrishnan, P.; Ganesan, P.; Manthiram, A.; Shanmugam, S. LaTi_{0.65}Fe_{0.35}O₃ – nanoparticle-decorated nitrogen-doped carbon nanorods as an advanced hierarchical air electrode for rechargeable metal-air batteries. *Nano Energy* **2015**, *15*, 92–103. [\[CrossRef\]](#)
47. Lima, A.; Lima, A.; Meloni, G.; Santos, C.; Bertotti, M. Perovskite-Type Oxides La_{0.6}M_{0.4}Ni_{0.6}Cu_{0.4}O₃ (M = Ag, Ba, Ce) towards the Oxygen Reduction Reaction (ORR) in Alkaline Medium: Structural Aspects and Electrocatalytic Activity. *J. Braz. Chem. Soc.* **2021**, *32*, 665–674. [\[CrossRef\]](#)
48. Lee, D.U.; Park, H.W.; Park, M.G.; Ismayilov, V.; Chen, Z. Synergistic Bifunctional Catalyst Design based on Perovskite Oxide Nanoparticles and Intertwined Carbon Nanotubes for Rechargeable Zinc–Air Battery Applications. *ACS Appl. Mater. Interfaces* **2015**, *7*, 902–910. [\[CrossRef\]](#)
49. Zheng, Q.; Zhang, Y.; Wang, C.; Zhang, C.; Guo, Y. CoO Enhanced Oxygen Evolution Kinetics of LaMnO₃ Perovskite As a Potential Cathode for Rechargeable Zn–Air Batteries. *Energy Fuels* **2022**, *36*, 1091–1099. [\[CrossRef\]](#)
50. Wang, X.; Sunarso, J.; Lu, Q.; Zhou, Z.; Dai, J.; Guan, D.; Zhou, W.; Shao, Z. High-Performance Platinum-Perovskite Composite Bifunctional Oxygen Electrocatalyst for Rechargeable Zn–Air Battery. *Adv. Energy Mater.* **2020**, *10*, 1903271. [\[CrossRef\]](#)
51. Flores-Lasluisa, J.X.; Huerta, F.; Cazorla-Amorós, D.; Morallón, E. Manganese oxides/LaMnO₃ perovskite materials and their application in the oxygen reduction reaction. *Energy* **2022**, *247*, 123456. [\[CrossRef\]](#)
52. Zeng, K.; Li, C.; Lu, J.; Sun, J.; Pan, X.; Jin, C.; Wei, M.; Yang, R. A-Site Doped Perovskite Oxide Strongly Interface Coupling with Carbon Nanotubes as a Promising Bifunctional Electrocatalyst for Solid-State Zn–Air Batteries. *Energy Fuels* **2021**, *35*, 12700–12705. [\[CrossRef\]](#)
53. Flores-Lasluisa, J.X.; Huerta, F.; Cazorla-Amorós, D.; Morallón, E. Structural and morphological alterations induced by cobalt substitution in LaMnO₃ perovskites. *J. Colloid Interface Sci.* **2019**, *556*, 658–666. [\[CrossRef\]](#) [\[PubMed\]](#)
54. Mathumba, P.; Fernandes, D.M.; Matos, R.; Iwuoha, E.I.; Freire, C. Metal Oxide (Co₃O₄ and Mn₃O₄) Impregnation into S, N-doped Graphene for Oxygen Reduction Reaction (ORR). *Materials* **2020**, *13*, 1562. [\[CrossRef\]](#) [\[PubMed\]](#)
55. Waseda, Y.; Matsubara, E.; Shinoda, K. *X-ray Diffraction Crystallography*; Springer: Berlin/Heidelberg, Germany, 2011. [\[CrossRef\]](#)
56. Thommes, M.; Kaneko, K.; Neimark, A.V.; Olivier, J.P.; Rodriguez-Reinoso, F.; Rouquerol, J.; Sing, K.S.W. Physisorption of gases, with special reference to the evaluation of surface area and pore size distribution (IUPAC Technical Report). *Pure Appl. Chem.* **2015**, *87*, 1051–1069. [\[CrossRef\]](#)
57. Risch, M. Perovskite electrocatalysts for the Oxygen reduction reaction in alkaline media. *Catalysts* **2017**, *7*, 154. [\[CrossRef\]](#)
58. Bu, Y.; Jang, H.; Gwon, O.; Kim, S.H.; Joo, S.H.; Nam, G.; Kim, S.; Qin, Y.; Zhong, Q.; Kwak, S.K.; et al. Synergistic interaction of perovskite oxides and N-doped graphene in versatile electrocatalyst. *J. Mater. Chem. A* **2019**, *7*, 2048–2054. [\[CrossRef\]](#)
59. Sunding, M.F.; Hadidi, K.; Diplas, S.; Løvvik, O.M.; Norby, T.E.; Gunnaes, A.E. XPS characterisation of in situ treated lanthanum oxide and hydroxide using tailored charge referencing and peak fitting procedures. *J. Electron Spectros. Relat. Phenom.* **2011**, *184*, 399–409. [\[CrossRef\]](#)
60. Mondal, P.; Bhattacharya, D.; Maity, A.; Chakrabarti, O.; Maidul Islam, A.K.M.; Mukherjee, M. Evolution of orbital phases with particle size in nanoscale stoichiometric LaMnO₃. *J. Appl. Phys.* **2011**, *109*, 084327. [\[CrossRef\]](#)
61. Okamoto, Y.; Nakano, H.; Imanaka, T.; Teranishi, S. X-ray Photoelectron Spectroscopic Studies of Catalysts—Supported Cobalt Catalysts—. *Bull. Chem. Soc. Jpn.* **1975**, *48*, 1163–1168. [\[CrossRef\]](#)

62. Elsiddig, Z.A.; Xu, H.; Wang, D.; Zhang, W.; Guo, X.; Zhang, Y.; Sun, Z.; Chen, J. Modulating Mn^{4+} Ions and Oxygen Vacancies in Nonstoichiometric $LaMnO_3$ Perovskite by a Facile Sol-Gel Method as High-Performance Supercapacitor Electrodes. *Electrochim. Acta* **2017**, *253*, 422–429. [CrossRef]
63. Oku, M.; Hirokawa, K.; Ikeda, S. X-ray photoelectron spectroscopy of manganese—Oxygen systems. *J. Electron Spectros. Relat. Phenom.* **1975**, *7*, 465–473. [CrossRef]
64. Zhao, Y.; Hang, Y.; Zhang, Y.; Wang, Z.; Yao, Y.; He, X.; Zhang, C.; Zhang, D. Strontium-doped perovskite oxide $La_{1-x}Sr_xMnO_3$ ($x = 0, 0.2, 0.6$) as a highly efficient electrocatalyst for nonaqueous $Li-O_2$ batteries. *Electrochim. Acta* **2017**, *232*, 296–302. [CrossRef]
65. Lv, Y.; Li, Z.; Yu, Y.; Yin, J.; Song, K.; Yang, B.; Yuan, L.; Hu, X. Copper/cobalt-doped $LaMnO_3$ perovskite oxide as a bifunctional catalyst for rechargeable $Li-O_2$ batteries. *J. Alloys Compd.* **2019**, *801*, 19–26. [CrossRef]
66. Gautier, J.L.; Rios, E.; Gracia, M.; Marco, J.F.; Gancedo, J.R. Characterisation by X-ray photoelectron spectroscopy of thin $Mn_xCo_{3-x}O_4$ ($1 \geq x \geq 0$) spinel films prepared by low-temperature spray pyrolysis. *Thin Solid Films* **1997**, *311*, 51–57. [CrossRef]
67. Assumpção, M.H.M.T.; De Souza, R.F.B.; Rascio, D.C.; Silva, J.C.M.; Calegari, M.L.; Gaubeur, I.; Paixão, T.R.L.C.; Hammer, P.; Lanza, M.R.V.; Santos, M.C. A comparative study of the electrogeneration of hydrogen peroxide using Vulcan and Printex carbon supports. *Carbon* **2011**, *49*, 2842–2851. [CrossRef]
68. Pargoletti, E.; Salvi, A.; Giordana, A.; Cerrato, G.; Longhi, M.; Minguzzi, A.; Cappelletti, G.; Vertova, A. ORR in Non-Aqueous Solvent for Li-Air Batteries: The Influence of Doped MnO_2 -Nanoelectrocatalyst. *Nanomaterials* **2020**, *10*, 1735. [CrossRef]
69. Flores-Lasluisa, J.X.; Huerta, F.; Cazorla-Amorós, D.; Morallón, E. $LaNi_{1-x}Co_xO_3$ perovskites for application in electrochemical reactions involving molecular oxygen. *Energy* **2023**, *273*, 127256. [CrossRef]
70. Bulavchenko, O.A.; Gerasimov, E.Y.; Afonasev, T.N. Reduction of double manganese–cobalt oxides: In situ XRD and TPR study. *Dalt. Trans.* **2018**, *47*, 17153–17159. [CrossRef] [PubMed]
71. Garces, L.J.; Hincapié, B.; Zenger, R.; Suib, S.L. The Effect of Temperature and Support on the Reduction of Cobalt Oxide: An in Situ X-ray Diffraction Study. *J. Phys. Chem. C* **2015**, *119*, 5484–5490. [CrossRef]
72. Salman, A.U.R.; Hyrve, S.M.; Regli, S.K.; Zubair, M.; Enger, B.C.; Lødeng, R.; Waller, D.; Rønning, M. Catalytic Oxidation of NO over $LaCo_{1-x}B_xO_3$ ($B = Mn, Ni$) Perovskites for Nitric Acid Production. *Catalysts* **2019**, *9*, 429. [CrossRef]
73. Abrego-Martínez, J.C.; Wang, Y.; Moreno-Zuria, A.; Wei, Q.; Cuevas-Muñiz, F.M.; Arriaga, L.G.; Sun, S.; Mohamedi, M. Nanostructured $Mn_2O_3/Pt/CNTs$ selective electrode for oxygen reduction reaction and methanol tolerance in mixed-reactant membraneless micro-DMFC. *Electrochim. Acta* **2019**, *297*, 230–239. [CrossRef]
74. Celorrio, V.; Dann, E.; Calvillo, L.; Morgan, D.J.; Hall, S.R.; Fermin, D.J. Oxygen Reduction at Carbon-Supported Lanthanides: The Role of the B-Site. *ChemElectroChem* **2016**, *3*, 283–291. [CrossRef]
75. Vignesh, A.; Prabu, M.; Shanmugam, S. Porous $LaCo_{1-x}Ni_xO_{3-\delta}$ Nanostructures as an Efficient Electrocatalyst for Water Oxidation and for a Zinc–Air Battery. *ACS Appl. Mater. Interfaces* **2016**, *8*, 6019–6031. [CrossRef] [PubMed]
76. Wang, J.; Zhao, C.-X.; Liu, J.-N.; Ren, D.; Li, B.-Q.; Huang, J.-Q.; Zhang, Q. Quantitative kinetic analysis on oxygen reduction reaction: A perspective. *Nano Mater. Sci.* **2021**, *3*, 313–318. [CrossRef]
77. Hona, R.K.; Ramezanipour, F. Remarkable Oxygen-Evolution Activity of a Perovskite Oxide from the $Ca_{2-x}Sr_xFe_2O_{6-\delta}$ Series. *Angew. Chemie* **2019**, *131*, 2082–2085. [CrossRef]
78. The Leading Metals Information Provider. Available online: <https://www.metal.com/> (accessed on 13 February 2024).

Disclaimer/Publisher’s Note: The statements, opinions and data contained in all publications are solely those of the individual author(s) and contributor(s) and not of MDPI and/or the editor(s). MDPI and/or the editor(s) disclaim responsibility for any injury to people or property resulting from any ideas, methods, instructions or products referred to in the content.